



Ni/amorphous CuO core–shell nanocapsules with enhanced electrochemical performances



Xianguo Liu^{a,*}, Yuping Sun^b, Chao Feng^a, Chuangui Jin^a, Feng Xiao^a

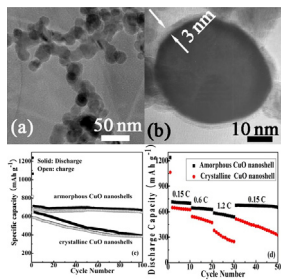
^aSchool of Materials Science and Engineering, Anhui University of Technology, Ma'anshan 243002, PR China

^bCenter for Engineering Practice and Innovation Education, Anhui University of Technology, Ma'anshan 243002, PR China

HIGHLIGHTS

- Ni/amorphous CuO core–shell nanocapsules have been prepared.
- Amorphous CuO nanoshell leads to improved stability and electrochemical performances.
- Ni/CuO nanocapsules maintain a reversible capacity of 673.4 mAh g⁻¹ over 100 cycles.

GRAPHICAL ABSTRACT



ARTICLE INFO

Article history:

Received 1 June 2013

Received in revised form

23 June 2013

Accepted 25 June 2013

Available online 2 July 2013

Keywords:

Core–shell

Amorphous

Anode

Lithium-ion batteries

ABSTRACT

A new type of core–shell nanocapsules with Ni nanoparticles as cores and amorphous CuO as shells have been synthesized through the arc-discharge method and subsequently annealing process. Amorphous CuO nanoshells lead to the improved stability and electrochemical performances. When evaluated as anode materials for lithium-ion batteries, the Ni/amorphous CuO nanocapsules deliver an initial discharge capacity of 1238.4 mAh g⁻¹ at 100 mA g⁻¹ and maintain a higher reversible capacity of 673.4 mAh g⁻¹ over 100 cycles, compared to the Ni/crystalline CuO nanocapsules (392 mAh g⁻¹). The feasibility of this material in lithium-ion batteries will offer guidelines for the future design of new materials with optimum properties and beneficial structural elements to realize improvements in electrochemical performances.

© 2013 Elsevier B.V. All rights reserved.

1. Introduction

Transition-metal oxides are promising high-performance materials for next-generation lithium-ion batteries (LIBs) because of their high energy density and high voltage [1–3]. Among the metal oxides, CuO has been considered as a promising candidate due to its high theoretical capacity (674 mAh g⁻¹), abundance, low cost, intrinsic thermal safety, and environmental compatibility [3–6].

However, its low conductivity and morphological collapse by the large volume increases during the charge/discharge cycles leading to poor cyclability and a low capacity at high C-rates [7–9]. The morphology and size of CuO have the significant influence on the electrochemical performances. In nano-structured CuO, not only is lithium diffusion much easier, but also the strain associated with lithium uptake can be well accommodated, leading to better electrochemical performances than the conventional materials [10]. Multifarious CuO nanostructures, such as nanourchins, nanoleaves, nanoneedles, nanoflowers and hollow nanostructures have been prepared [3,7,11–14]. Although the nano-structured CuO electrode can show high discharge capacity and good

* Corresponding author.

E-mail address: liuxianguohugh@gmail.com (X. Liu).

cycling performance at low rate, the initial coulombic efficiency and cycling stability at high rate are still disappointing. Amorphous metal oxides have been reported as a promising candidate for anode materials, because of their remarkable battery performance at high current rates [15–20]. Core–shell structured nanocapsules are a special type of nanoparticles, which are usually composed of cores and shells of nanometer size that are made of different materials [21]. Core–shell structured nanocapsules have been widely applied in anode materials to markedly improve the cycling behavior and the kinetics of lithium intercalation and de-intercalation in composites [22–24].

This work reports on the synthesis of core–shell Ni/amorphous CuO nanocapsules and their application as anode materials for LIBs. The reasons for which we choose Ni/amorphous CuO nanocapsules as anodes for LIBs are: (i) compared with crystalline nanomaterials, amorphous nanomaterials show the advantage of a low temperature synthetic procedure, as well as providing reliable continuous pathways for Li^+ during the charge–discharge process [16,17,25]; (ii) the nanoshells reduce the traveling path for electrons and Li^+ ions, facilitating Li^+ ion exchange across the interfaces, and tolerate the large volume change in the electrodes during the course of extraction and insertion of Li^+ ions, enhancing the kinetics and structural stability for lithium storage [17,19,20]; (iii) since CuO is a typical p-type semiconductor with band gap of 1.2 eV, while metallic Ni is a good conductor. The Ni cores can enhance the conductivity of CuO nanoshells electrode [14].

2. Experimental

2.1. Material preparation procedure

The used modified arc-discharge method has been described in detail in our previous work [26,27]. In brief, a $\text{Ni}_{92}\text{Cu}_8$ (at.%) ingot serves as the anode, while the cathode is a tungsten needle. The anode target is placed into a water-cooled copper crucible. After the chamber is evacuated (in a vacuum of 1.0×10^{-2} Pa), a mixture of argon of 1.6×10^4 Pa and hydrogen of 0.4×10^4 Pa are introduced into the chamber. The arc-discharge current is maintained at 80 A for 4 h to evaporate alloys sufficiently. Then the product in the form of powder is collected, after passivated for 8 h in the air. To prepare the Ni/amorphous CuO nanocapsules and Ni/crystalline CuO nanocapsules, we anneal the products at 150 and 300 °C for 0.5 h in a tubular furnace in still air, respectively.

2.2. Materials characterization

The composition and phase purity of the as-synthesized samples are analyzed by X-ray diffraction (XRD), acquired by a Bruker D8 Advance X-ray diffractometer equipped with a monochromatized Cu-K_α radiation. Transmission electron microscopy (TEM) and high-resolution TEM (HRTEM) images are obtained on a JEOL JEM-2010 transmission electron microscope at an acceleration voltage of 200 kV. The surface composition is analyzed by a X-ray photoelectron spectroscopy (XPS) spectrometer, using Mg K_α line (1253.6 eV) excitation (Perkin–Elmer PHI 1600 ESCA system). Brunauer–Emmett–Teller (BET) surface area measurements are performed with a Micromeritics ASAP-2000 nitrogen adsorption apparatus.

2.3. Electrode fabrication and electrochemical measurements

Electrochemical experiments are carried out by using standard CR2032 type coin cells. The working electrodes are prepared by mixing the CuO nanocapsules, carbon black and poly(vinyl difluoride) (PVDF) at weight ratio of 80:10:10 and pasted on a pure

Cu foil. A metallic lithium foil serves as the counter electrode, 1 M LiPF₆ in ethylene carbonate (EC)–dimethyl carbonate (DMC) (1:1 in volume) is used as the electrolyte. The cells are assembled in an argon-filled glove box. The galvanostatic charge–discharge tests are performed on a land battery program-control test system (Wuhan, China) between 5 mV and 3.0 V at room temperature. The cyclic voltammetry (CV) test is carried out on an electrochemical workstation (Model 2273, Princeton Applied Research, USA) in the potential window of 0.005–3.0 V (vs. Li/Li^+) at a scan rate of 0.2 mV s⁻¹. Electrochemical impedance spectroscopy (EIS) measurements are performed on this apparatus using a three-electrode cell with the metallic lithium foil as both the counter and reference electrodes over a frequency range of 100 kHz–10 MHz at different charge–discharge stages by applying an AC signal of 5 mV.

3. Results and discussion

XRD pattern in Fig. 1 shows the phase components of the products synthesized after the annealing process at 150 °C for 0.5 h in air. All sharp reflection peaks could be indexed to Ni with the body-centered-cubic structure. It is noteworthy that no Ni oxides peaks are detectable in the XRD patterns, indicating that the core of the nanocapsules may be free from oxidation, due to the protective shell. Compared with the standard card (PDF#70-1849), all reflection peaks shift to high angles, suggesting that Cu as the solid-solution atom enters into the Ni lattice due to similar radius of Ni (1.62 Å) and Cu (1.57 Å) atoms. In the XRD pattern, there are no detectable peaks for Cu oxides, indicating the Cu oxides are in small amount in the nanocapsules. Also the CuO which forms the shell of the nanocapsules is difficult to detect in the XRD pattern because of the periodic boundary condition (translation symmetry) along the radial direction has been broken down [28,29]. The XRD patterns of the products annealed at 300 °C for 0.5 h in air can also be indexed as Ni. With an increase in the annealing temperature up to 300 °C, there are gradual increase in the intensity and narrow in diffraction peaks, indicating the growth of Ni nanoparticles.

In Fig. 2a, the morphology, size distribution and core/shell structure of the products synthesized after the annealing process at 150 °C for 0.5 h in air are investigated by TEM. Most of the nanocapsules as-prepared are irregular sphere shape with the narrow distribution of diameters, ranging from 10 to 40 nm. The averaged diameter is about 27.8 nm, after averaging that of more than 100 nanocapsules, which is consistent with 22.4 nm calculated from the XRD (111) peak according to the Scherrer equation. In Fig. 2b, the HRTEM image clearly shows the shell/core structure with a

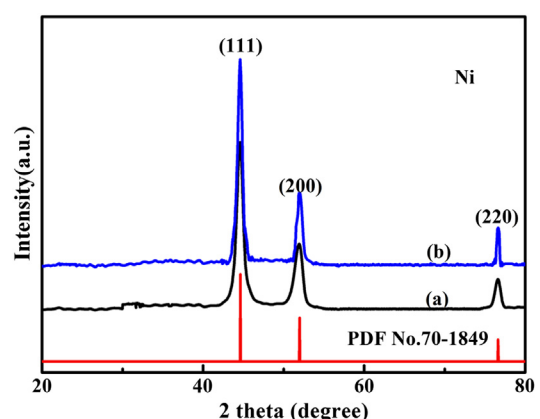


Fig. 1. XRD patterns of (a) products annealed at 150 °C for 0.5 h in air and (b) products annealed at 300 °C for 0.5 h in air.

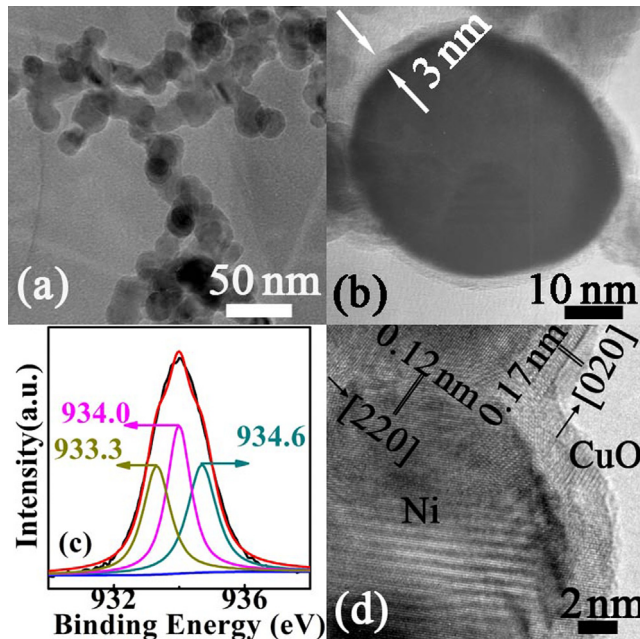


Fig. 2. (a) TEM and (b) HRTEM images and (c) XPS spectrum and the corresponding fitting curves of the Cu 2p3/2 electrons on the surface of the products synthesized after the annealing process at 150 °C for 0.5 h in air. (d) HRTEM image of the products synthesized after the annealing process at 300 °C for 0.5 h in air.

crystalline core and an amorphous shell with 3 nm thickness. In order to obtain more information, we investigate the nanocapsules with XPS. The XPS curve of Cu 2p3/2 on the surface of nanocapsules is shown in detail in Fig. 1c. The shells of the nanocapsules can be determined as CuO from the binding energy peak of 933.3, 934.0 and 934.6 eV [30–32] using the Lorentzian–Gaussian product function [33]. The products synthesized after the annealing process at 150 °C for 0.5 h in air can be determined to be Ni/amorphous CuO nanocapsules. A typical HRTEM image of the products synthesized after the annealing process at 300 °C for 0.5 h in air, as shown in Fig. 2d, clearly shows that it has the core/shell type of structure with a crystalline core and a crystalline shell. In the crystalline core, the d-spacing of 0.12 nm corresponds to the lattice distance of {220} planes of Ni. In the crystalline shell, the fringe spacing of 0.17 nm corresponds to the {020} planes of CuO. The products synthesized after the annealing process at 300 °C for 0.5 h in air are the Ni/crystalline CuO nanocapsules. The BET surface areas of the Ni/amorphous CuO nanocapsules and Ni/crystalline CuO nanocapsules are 96.2 and 34.4 m² g⁻¹, respectively, which is consistent with the XRD results. The large specific area for amorphous nanoshells is beneficial for the improved electrochemical properties.

The phenomena above can be ascribed to the formation mechanism of the nanocapsules. i.e., different evaporating pressures, melting points for Ni and Cu atoms, during the arc discharging process [33]. For an evaporating pressure of 1.33×10^{-3} Pa, the corresponding evaporating temperature is 1157 °C for Ni and 937 °C for Cu. The melting points of Ni and Cu are 1453 and 1085 °C, respectively. The formation process of the nanocapsules synthesized by the arc discharge can be classified into evaporation of Ni, Cu and their vapor condensation. When the Ni₉₂Cu₈ ingot is evaporated to be the liquid of Ni₉₂Cu₈ alloys by the plasma with several thousand degrees, Cu atoms with the low evaporating temperature 937 °C take the priority to evaporate and then bump up each other between Ni and Cu atoms, but a small amount of Cu atoms enter into the Ni lattice as the solid-solution atoms, due to the same structure and similar atom size. It can be suggested that in

the condensation process, atoms of elements Cu and Ni move out from the plasma, as the temperature is at several thousand degrees. When the temperature is decreased, the Ni solid-solution with the high melting point 1453 °C firstly forms nucleus and the Cu atoms are near them. By the end, these Cu atoms are abounded on the surface of the Ni solid-solution nanoparticles, in which core–shell structure can be formed. When the products are exposed to air, Cu atoms are easily oxidized to amorphous Cu oxides on the surfaces of the nanocapsules, due to the high surface energy on the nano-material. The products are annealed at 150 °C for 0.5 h in a tubular furnace in still air to make amorphous Cu oxides to form amorphous CuO nanoshells. When the annealing temperature reaches at 300 °C, the amorphous CuO nanoshells transform to be crystalline CuO nanoshells.

The CV curves of the 1st, 2nd and the 10th cycle of two samples between 5 mV and 3 V at a scan rate of 0.2 mV s⁻¹ are shown in Fig. 3a. For two samples, the great difference in shape of the curve between the first cycle and subsequent cycles can be attributed to the irreversible process occurred during the initial cycle [34]. For the Ni/crystalline CuO nanocapsules, three cathodic peaks at 1.95, 0.97 and 0.72 V during the first reduction scan, mainly correspond to reductive reaction from CuO to Cu₂O, the decomposition of Cu₂O into CuO and Li₂O, and further decomposition into Cu and Li₂O, respectively [12,35]. The anodic peaks at 1.50 and 2.56 V appearing in the first oxidation scan, which are related to the oxidation process $2\text{Cu} + \text{Li}_2\text{O} \rightarrow \text{Cu}_2\text{O} + 2\text{Li}$ and the oxidation of Cu₂O to CuO, respectively [12]. In the first cycle, the area of the cathodic and anodic peaks of Ni/amorphous CuO nanocapsules are more closed than that of Ni/crystalline CuO nanocapsules. Smaller the difference in the areas of cathodic and anodic peaks indicates the higher coulombic efficiency of the electrode [14]. That is to say, the initial coulombic efficiency of amorphous CuO nanoshells is higher than that of crystalline CuO nanoshells [14]. The areas of all CV peaks of Ni nanocapsules with amorphous CuO nanoshells are larger than those of Ni nanocapsules with crystalline CuO nanoshells, indicating more reactions toward Li⁺ occur in amorphous CuO nanoshells [12]. It is attributed to the amorphous state, which acts as nervures to facilitate Li⁺ transfer on active material/electrolyte interfaces, ensuring the improved electrical contact of CuO/CuO and CuO/current collector [12]. The improved electric conductivity of the amorphous CuO nanoshells can enhance the kinetics and the extent of electrode reactions. Compared with the Ni/crystalline CuO nanocapsules, the cathodic peaks of Ni/amorphous CuO nanocapsules shift to higher potential, and the anodic peaks shift to lower potential, which indicates that the amorphous CuO nanoshells facilitate Li₂O decomposition and reaction $\text{CuO} + 2\text{Li}^+ + 2\text{e}^- \rightarrow \text{Cu} + \text{Li}_2\text{O}$. Obviously, the separations between the cathodic and anodic peaks of the Ni/amorphous CuO nanocapsules electrode decrease as compared to the Ni/crystalline CuO nanocapsules electrode, which indicates the weaker polarization of Ni/amorphous CuO nanocapsules electrode. The improvement of the electric conductivity can reduce the polarization and improve the reversibility of the electrode [14]. In addition, it can be seen that in the 10th scan, the peak intensity is nearly unchanged and the reduction peaks are located at 2.36, 1.31 and 0.68 V in Ni/amorphous CuO nanocapsules, indicating the electrode reactions more reversible.

Fig. 3b and c display the discharge–charge curves for the 1st, 2nd, 50th and 100th cycle of two samples electrode measured at a current density of 100 mA g⁻¹ (1C = 670 mA g⁻¹). The initial discharge capacities of the Ni/crystalline CuO and Ni/amorphous CuO nanocapsules are 1238.4 and 1064.2 mAh g⁻¹, respectively. These values are much higher than the theoretic capacity (674 mAh g⁻¹), attributed to the formation of SEI film during the discharge process [34]. The initial coulombic efficiency of Ni/crystalline CuO nanocapsules is

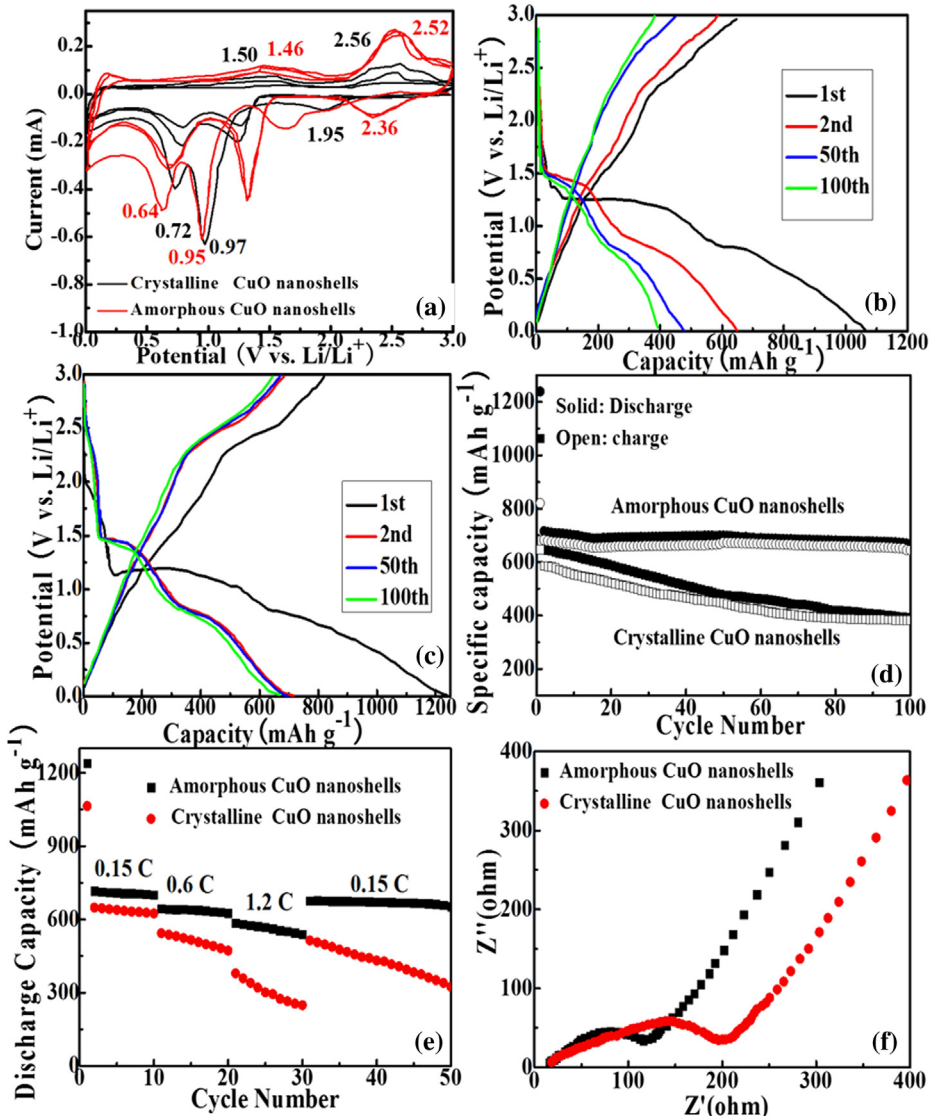


Fig. 3. (a) CV curves of two samples for the first, the second and the 10th cycle. Scan rate: 0.2 mV s^{-1} , potential range: $0.005\text{--}3.0 \text{ V}$; Typical galvanostatic charge–discharge curves of (b) Ni/crystalline CuO nanocapsules and (c) Ni/amorphous CuO nanocapsules between 0.005 and 3 V vs. Li at constant current density of 100 mA g^{-1} . (d) Cycling performance of two samples electrodes at current density of 100 mA g^{-1} . (e) Discharge capacity of two samples electrode at different discharge–charge rates (0.15 , 0.6 and 1.2C). (f) Nyquist plots of two samples electrodes obtained by applying a sine wave with amplitude of 5.0 mV over frequency range $100 \text{ kHz}\text{--}10 \text{ MHz}$.

60.6% (the initial charge capacity is 645 mAh g^{-1}) in Fig. 3b and the Ni/amorphous CuO nanocapsules exhibit an initial coulombic efficiency of 66.2% (the initial charge capacity is 820.2 mAh g^{-1}) in Fig. 3c. Generally, the main causes of the initial irreversible capacity of transition oxides are the formation of SEI film on surface and the incomplete decomposition of Li_2O during the first cycle [22]. The reversible capacity of the Ni/amorphous CuO nanocapsules over the 100th cycle is 673.4 mAh g^{-1} , which is higher than the Ni/crystalline CuO nanocapsules of 392 mAh g^{-1} . In addition, the reversible capacity of the Ni/amorphous CuO nanocapsules is nearly unchanged from the 2nd cycle to the 100th cycle. It is clear that the Ni/amorphous CuO nanocapsules have much better cycling performance compared to the Ni/crystalline CuO nanocapsules, which is attributed to the facile Li^+ ion diffusion through the amorphous CuO nanoshells and a suppression of the side reactions between the amorphous CuO nanoshells and electrolyte.

The cycling performances of two samples are shown in Fig. 3d. As expected, the Ni/amorphous CuO nanocapsules anode exhibits

much better cyclic stability than that of the Ni/crystalline CuO nanocapsules anode. The capacity of the Ni/amorphous CuO nanocapsules maintain at 673.4 mAh g^{-1} (94.1% capacity of the 2nd cycle) over 100 cycles with a high Coulombic efficiency of $\sim 94.1\%$, while the capacity of Ni/crystalline CuO nanocapsules can sustain 60.4% (392 mAh g^{-1}) capacity of the 2nd cycle. The high reversible capacity of Ni/amorphous CuO nanocapsules can be attributed to the core/shell structure. Amorphous CuO nanoshells not only provide large specific surface area for the intercalation of lithium ions, and but also contain many structural defects to accommodate lithium ions.

As shown in Fig. 3e, it is clearly noted that Ni/amorphous CuO nanocapsules hold the outstanding high-rate performance when compared with Ni/crystalline CuO nanocapsules. For the Ni/amorphous CuO nanocapsules, reversible capacity decreases slowly with the increase of discharge–charge rates, and a rate capacity of 1238.4 , 644 and 585 mAh g^{-1} can be obtained at rates of 0.15 , 0.6 and 1.2C , successively. Their capacities are all higher than those of the Ni/crystalline CuO nanocapsules at each rate. Upon decreasing the rate

to 0.15C, the reversible capacity reached 676 mAh g⁻¹. Additionally, after another 20 cycles at the 0.15C rates, the Ni/amorphous CuO electrode still delivers a discharge capacity of 652 mAh g⁻¹, corresponding to 96.4% capacity retention of the initial discharge capacity of 676 mAh g⁻¹. The capacity and cycle performance of Ni/amorphous CuO nanocapsules are also found to be higher than those of the reported CuO nanomaterials [7–16,36,37]. The electrochemical impedance spectra of the two samples are shown in Fig. 3f. Each of them shows a high-frequency semicircle, a medium frequency semicircle, and a low-frequency inclined line, which is typical for the existence of SEI film, the charge-transfer and double layer, and the lithium-diffusion process within electrodes, respectively [37,38]. Obviously, the Ni/amorphous CuO electrode shows lower impedance than that of Ni/crystalline CuO electrode. This can explain the lower polarization and superior rate performance of the Ni/amorphous CuO nanocapsules. Li ion diffusion cannot be restricted by any defects in the amorphous phase which is considered conceptually defect-free phase [39]. To some extent, the amorphous compounds can also be compared with electron-conducting polymers, or redox polymers [40]. The crystalline CuO nanoshells with many defects are not ideal crystalline one. The clear mechanism of electron conduction is not yet understood and is further studied.

To understand the effect of amorphous CuO nanoshells in enhancing the electrochemical behavior, the morphology and microstructure variation of two samples are examined using TEM after 100 discharge/charge cycles, as shown in Fig. 4. It is apparent from the postmortem analysis that the morphology of Ni/crystalline CuO nanocapsules (Fig. 4a), after 100 discharge/charge cycles, undergoes drastic change, both in terms of shape and size with substantially broken nanoparticles readily apparent. Fig. 4b clearly shows the crystalline CuO nanoshells still exist after 100 cycles. In contrast, the postmortem analysis of the Ni/amorphous CuO nanocapsules (Fig. 4c and d) demonstrates that Ni/amorphous CuO nanocapsules maintain the shape integrity and the CuO still keep the amorphous state after 100 cycles, which underscores the crucial role the amorphous CuO nanoshells played in mechanically stabilizing the material during repeated lithium insertion and

deinsertion reactions. Compared with crystalline metals or alloys, the Young's modulus of amorphous metals or alloys is lower, leading to the higher elastic strain limit [41]. It is apparent that high structural stability leads to the excellent cycling performance of Ni/amorphous CuO nanocapsules.

4. Conclusions

The present work has provided a method for the synthesis of a new type of nanocapsules with Ni nanoparticles as cores and amorphous CuO as shells. The proposed Ni/amorphous CuO nanocapsules is firstly prepared by an arc discharge method and subsequently by annealing at 150 °C for 0.5 h in Air. The Ni/amorphous CuO nanocapsules are further tested as an anode material for LIBs, exhibiting superior performance in terms of specific capacitance and cyclability. The Ni/amorphous CuO nanocapsules deliver an initial discharge capacity of 1238.4 mAh g⁻¹ at 100 mA g⁻¹ and maintain a higher reversible capacity of 673.4 mAh g⁻¹ over 100 cycles, compared to the Ni/crystalline CuO nanocapsules (392 mAh g⁻¹). All of these properties make this material a promising anode material for LIBs. The approach offers an effective route to improve the performance of highly insulating electrode materials for batteries.

Acknowledgments

This study was supported by the National Natural Science Foundation of China (grant nos. 51201002 and 51071001).

References

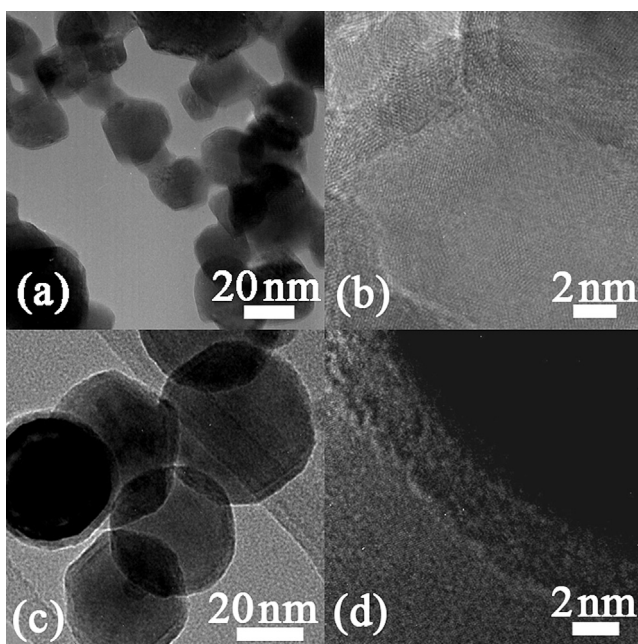


Fig. 4. TEM images of (a) Ni/crystalline CuO nanocapsules and (c) Ni/amorphous CuO nanocapsules after 100 discharge/charge cycles. HRTEM images of (b) Ni/crystalline CuO nanocapsules and (d) Ni/amorphous CuO nanocapsules after 100 cycles.

- [1] Z.Y. Wang, L. Zhou, X.W. Lou, *Adv. Mater.* 24 (2012) 1903–1911.
- [2] M. Armand, J.M. Tarascon, *Nature* 451 (2008) 652–657.
- [3] H.B. Wu, J.S. Chen, H.H. Hng, X.W. Lou, *Nanoscale* 4 (2012) 2526–2542.
- [4] S.Y. Gao, S.X. Yang, J. Shu, S.X. Zhang, Z.D. Li, K. Jiang, *J. Phys. Chem. C* 112 (2008) 19324–19328.
- [5] R. Sahay, P.S. Kumar, V. Aravindan, J. Sundaramurthy, W.C. Ling, S.G. Mhaisalkar, S. Ramakrishna, S. Madhavi, *J. Phys. Chem. C* 116 (2012) 18087–18092.
- [6] Z.Y. Wang, F.B. Su, S. Madhavi, X.W. Lou, *Nanoscale* 3 (2011) 1618–1623.
- [7] J.S. Zhou, L.L. Ma, H.H. Song, B. Wu, X.H. Chen, *Electrochim. Commun.* 13 (2009) 1357–1360.
- [8] W.M. Zhang, X.L. Wu, J.S. Hu, Y.G. Guo, L.J. Wan, *Adv. Funct. Mater.* 18 (2008) 3941–3946.
- [9] L. Zhi, Y.S. Hu, B.E. Hamaoui, X. Wang, I. Lieberwirth, U. Kolb, J. Maier, K. Müllen, *Adv. Mater.* 20 (2008) 1727–1731.
- [10] K.J. Zhao, M. Pharr, L. Hartle, J.J. Vlassak, Z.G. Suo, *J. Power Sources* 218 (2012) 6–14.
- [11] L.Q. Lu, Y. Wang, *Electrochim. Commun.* 14 (2012) 82–85.
- [12] J.Y. Xiang, J.P. Tu, J. Zhang, J. Zhong, D. Zhang, J.P. Cheng, *Electrochim. Commun.* 12 (2010) 1103–1107.
- [13] B. Zhao, P. Liu, H. Zhuang, Z. Jiao, T. Fang, W.W. Xu, B. Lu, Y. Jiang, *J. Mater. Chem. A* 1 (2013) 367–373.
- [14] J.Y. Xiang, J.P. Tu, Y.F. Yuan, X.L. Wang, X.H. Huang, Z.Y. Zeng, *Electrochim. Acta* 54 (2009) 1160–1165.
- [15] Y.N. Ko, S.H. Choi, Y.C. Kang, S.B. Park, *ACS Appl. Mater. Interfaces Commun.* 5 (2013) 3234–3240.
- [16] Z.H. Bi, M.P. Panthanaman, P.A. Menchhofer, R.R. Dehoff, C.A. Bridges, M.F. Chi, B.K. Guo, X.G. Sun, S. Dai, *J. Power Sources* 222 (2013) 461–466.
- [17] Y.L. Liu, Y.H. Xu, X.G. Han, C. Pellegrinelli, Y.J. Zhu, H.L. Zhu, J.Y. Wan, A.C. Chung, O. Vaaland, C.S. Wang, L.B. Hu, *Nano Lett.* 12 (2012) 5664–5668.
- [18] Z.Y. Wang, Z.C. Wang, W.T. Liu, W. Xiao, X.W. Lou, *Energy Environ. Sci.* 6 (2013) 87–91.
- [19] H. Wang, L.F. Cui, Y. Yang, H.S. Casalongue, J.T. Robinson, Y. Liang, Y. Cui, H. Dai, *J. Am. Chem. Soc.* 132 (2010) 13978–13980.
- [20] D. Wang, D. Choi, J. Li, Z. Yang, Z. Nie, R. Kou, D. Hu, C. Wang, L.V. Saraf, J. Zhang, I.A. Aksay, J. Liu, *ACS Nano* 3 (2009) 907–914.
- [21] X.G. Liu, D.Y. Geng, X.L. Wang, S. Ma, H. Wang, D. Li, B.Q. Li, W. Liu, Z.D. Zhang, *Chem. Commun.* 46 (2010) 6956–6958.
- [22] Z.G. Yin, Y.H. Ding, Q.D. Zheng, L.H. Guan, *Electrochim. Commun.* 20 (2012) 40–43.
- [23] P. Wu, N. Du, J. Liu, H. Zhang, J.X. Yu, D.R. Yang, *Mater. Res. Bull.* 46 (2011) 2278–2282.
- [24] N. Jayaprakash, W.D. Jones, S.S. Moganty, L.A. Archer, *J. Power Sources* 200 (2012) 53–58.

- [25] Y.J. Lee, A.M. Belcher, *J. Mater. Chem.* 21 (2011) 1033–1039.
- [26] X.G. Liu, J.J. Jiang, D.Y. Geng, B.Q. Li, Z. Han, W. Liu, Z.D. Zhang, *Appl. Phys. Lett.* 94 (2009) 053119.
- [27] X.G. Liu, D.Y. Geng, J. Du, S. Ma, B. Li, P.J. Shang, Z.D. Zhang, *Scr. Mater.* 59 (2008) 340–343.
- [28] X.G. Liu, B. Li, D.Y. Geng, W.B. Cui, F. Yang, Z.G. Xie, D.J. Kang, Z.D. Zhang, *Carbon* 47 (2009) 470–474.
- [29] X.G. Liu, Z.Q. Ou, D.Y. Geng, Z. Han, J.J. Jiang, W. Liu, Z.D. Zhang, *Carbon* 48 (2010) 891–897.
- [30] J.G. Jolley, G.G. Geesey, M.R. Haukins, R.B. Write, P.L. Wiehlacz, *Appl. Surf. Sci.* 37 (1989) 469–480.
- [31] T. Nakamura, H. Tomizuka, M. Takahashi, T. Hoshi, *J. Surf. Sci. Soc. Jpn.* 16 (1995) 515–524.
- [32] F. Parmigiani, G. Pacchioni, F. Illas, P.S. Bagus, *J. Electron Spectrosc. Relat. Phenom.* 59 (1992) 255–269.
- [33] D.Y. Geng, W.Y. Park, J.C. Kim, J.H. Yu, C.J. Choi, Z.D. Zhang, *J. Mater. Res.* 20 (2005) 2534–2543.
- [34] X.G. Liu, S.W. Or, C.G. Jin, Y.H. Lv, W.H. Li, C. Feng, F. Xiao, Y.P. Sun, *Electrochim. Acta* 100 (2013) 140–146.
- [35] A. Debart, L. Dupont, P. Poizot, D. Larcher, J.M. Tarascon, *J. Electrochem. Soc.* 148 (2001) A1266–A1274.
- [36] Q. Pan, M. Wang, Z. Wang, *Electrochim. Solid State Lett.* 12 (2009) A50–A53.
- [37] L.R. Zhao, H. Chen, Y.L. Wang, H.W. Che, P. Gunawan, Z.Y. Zhong, H. Li, F.B. Su, *Chem. Mater.* 24 (2012) 1136–1142.
- [38] Y.J. Mai, X.L. Wang, J.Y. Xiang, Y.Q. Qiao, D. Zhang, C.D. Gu, J.P. Tu, *Electrochim. Acta* 56 (2011) 2306–2311.
- [39] S.W. Kim, J. Ryu, C.B. Park, K. Kang, *Chem. Commun.* 46 (2010) 7409–7411.
- [40] C. Delacourt, P. Poizot, D. Bonnin, C. Masquelier, *J. Electrochem. Soc.* 156 (2009) A595–A605.
- [41] C.A. Schuh, T.C. Hufnagel, U. Ramamurthy, *Acta Mater.* 55 (2007) 4067–4109.